Combustion and Flame 159 (2012) 142–150

Contents lists available at ScienceDirect

Combustion and Flame

journal homepage: www.elsevier.com/locate/combustflame

Laminar counterflow steady diffusion flames under high pressure ($P \leqslant 3$ MPa) conditions

Lorenzo Figura, Alessandro Gomez *

Department of Mechanical Engineering, Yale Center for Combustion Studies, Yale University, New Haven, CT 06520-8286, USA

ARTICLE INFO

Article history:
Received 23 February 2011
Received in revised form 16 June 2011
Accepted 17 June 2011
Available online 21 July 2011

Keywords:
High pressure
Laminar
Diffusion flame
Counterflow

ABSTRACT

An experimental system was designed to stabilize steady counterflow methane diffusion flames at elevated pressures, up to 3 MPa. In contrast with the much more common coflow configuration, the counterflow one is advantageous for the following reasons: the suppression of buoyancy instabilities that typically plague coflow flames at high pressures; the one-dimensionality of the flame, that enables computational modeling with very large chemical kinetic mechanisms; and the high level of control that it provides on soot loading. Above 0.8 MPa, the replacement of nitrogen with helium as inert was found to be critical to stabilize well behaved flames with respect to steadiness, laminarity, adiabaticity, one-dimensionality and flame thickness. Scaling and experimental considerations allowed for the identification of acceptable operating conditions in terms of pressure and strain rate and yielded a synthetic representation of a domain of diffusion flames of good quality. Such a graph can inform the design of a high-pressure counterflow system with respect to the selection of burner geometry, diagnostic techniques and experimental conditions, allowing for the experimentalist to sidestep costly and time consuming trial and error. Measurements by thin-filament pyrometry and numerical simulations confirmed the proposed scaling.

1. Introduction

Despite the fact that extensive research has been conducted on laminar diffusion flames at atmospheric pressure for decades, work at elevated pressures has been rare [1–17]. Difficulties associated with high-pressure research include: cost, safety issues, instabilities, excessive soot load, and diagnostic challenges associated with a reduction in flame thickness, not to mention intrinsic difficulties with laser diagnostics (e.g., pressure-induced line broadening and beam steering). Nevertheless, high-pressure combustion is ubiquitous in practical applications and it is of primary importance to develop and test computational models with detailed transport and chemistry under pressure conditions of practical systems. In view of the strong dependence of transport properties on pressure and of the nonlinearity of Arrhenius kinetics, agreement between models and experiments at atmospheric conditions does not guarantee agreement at elevated pressures. Thus, establishing a well-controlled high-pressure experiment is desirable.

Of course, not to escalate the challenge, especially if additional complications such as soot formation and detailed pollutant modeling are among the objectives, one should consider first laminar flames. Most of the high-pressure research to date has been focused on soot studies in coflow flames. A typical outcome of these studies are valuable correlations between pressure and soot volume fraction, as in [1–6]. Despite the fact that pressures as high as 10 MPa can be reached [7], coflow experiments present the following problems:

(a) buoyancy instabilities may plague such flames even at relatively moderate pressure [8–10];
(b) flames can be made stable even at high pressures by operating at constant flow rate as the pressure rises [7], but at the cost of increased heat/mass losses to the burner rim that are difficult to quantify;
(c) the temperature-time history of a fluid parcels is streamline-dependent, adding complexity to the comparison of models and experiments;
(d) the two dimensional nature of the coflow flame makes it computationally taxing and less suited for testing chemical mechanism of great complexity, such as those involving soot formation/oxidation, though much progress has been made in this area (e.g. [18]); and
(e) the soot load may be difficult to control. Despite the fact that the complete oxidation of soot within the visible flame can be achieved with dilution, no soot-free or incipiently sooting flame has been stabilized at elevated pressures in a coflow flame with fuels of high soot propensity. Achieving such conditions is desirable, if the focus is on the long standing problem of soot inception that remains largely unsolved to date.

* Corresponding author. Fax: +1 203 432 7654.
E-mail address: alessandro.gomez@yale.edu (A. Gomez).

0010-2180/$ - see front matter © 2011 The Combustion Institute. Published by Elsevier Inc. All rights reserved.
doi:10.1016/j.combustflame.2011.06.013

To overcome some of these difficulties, different research groups have tried to stabilize high-pressure *counterflow* diffusion flames, with a focus on soot studies and strain rate effect [12–15], on chemical mechanism validation [16] or on global extinction [17]. The highest reported pressure in these experiments is 1.5 MPa [16]. The main advantage of the counterflow configuration is the ability to control the residence time of the reactant by acting on the strain rate. If the counterflow flame behaves one-dimensionally close to the centerline—a condition that is easily verifiable by visual inspection, numerical simulations require modest computational power and can be tackled with readily accessible commercial codes [19].

For the flame to be a useful test reactor, laminarity and steadiness are minimal requirements. Additionally, for observations to be of broad applicability, temperature and species profiles must have zero-gradient at the boundaries. Finally, as pressure increases, the flame becomes thinner and spatial resolution requirements for temperature and chemical species measurements pose new challenges.

To establish the correct range of experimental conditions in a fairly broad parameter space and fulfill all four requirements, laminarity, steadiness, adiabaticity and maximal flame thickness, we first review stability constraints of laminar flames, making a case for the relative advantage of using the counterflow configuration. Next, we present scaling laws from first principles, with the purpose of facilitating the design (combustor geometry, flow rates, etc.) of a high-pressure system. After describing in detail the experimental system, we demonstrate the stabilization of steady counterflow laminar diffusion flames up to 30 atm. By varying the strain rate and dilution level, blue and incipiently sooting flames were obtained in the pressure range of modern gas turbines. To reach the highest pressures, helium was substituted to nitrogen as inert. We then validate the scaling laws, and extend them to account for realistic composition of the feed streams, with temperature measurements performed by thin filament pyrometry [20] and compared with numerical simulations using Oppdif [19] and the GRI 3.0 mechanism [21]. We conclude by showing a graph of the operating conditions under which a well behaved flame can be stabilized. Once a suitable flame for a high-pressure study is identified, such a tool may help ascertaining whether the flame is well behaved apriori, that is, *before* the experimental arrangement and the diagnostics are selected. This predictability is one of the objectives of the present contribution to eliminate costly and time consuming trial and error.

2. Instabilities in laminar diffusion flames: coflow *vs.* counterflow

2.1. Coflow (jet) diffusion flames

The relevant scaling is based on the Richardson number, *Ri* that can be also expressed in terms of the Grashof number, *Gr* and the Reynolds number Re as

$$Ri = \frac{Gr}{\mathrm{Re}^2} = \frac{gL^3\Delta T}{v^2\bar{T}} \cdot \frac{v^2}{u^2 d^2} \tag{1}$$

where g is the gravitational acceleration, $\Delta T/\bar{T}$ is a variable of unity order with very modest dependence on pressure, representing the ratio of a characteristic temperature difference driving the buoyant flow over a mean temperature, d is the burner diameter and L is the characteristic vertical length over which buoyancy is acting, that is on the order of the flame height. Within a factor $\Delta T/\bar{T}$, *Ri* is equal to the inverse of the Froude number. In principle, one may want this number to be much larger (smaller) than unity, for buoyancy (inertia) to be controlling. Despite the fact that the flame height scales with fuel flow rate, which would suggest momentum control, laminar jet diffusion flames are typically buoyancy controlled, as conclusively shown by Roper in a number of papers [22–24]. Typically, these flames are elongated with $L/D \geqslant 5$–10 and $Ri \gg 1$ because of its cubic dependence on L.

Whether either buoyancy or inertia is controlling matters primarily to ascertain which instability affects the flame. If inertia is controlling, transition to eventually turbulent conditions is of concern. Transition may occur in the pipe flow within the burner at $\mathrm{Re} \cong 2300$, a number that is not iron cast and that can be increased by careful flow conditioning. Or, it may appear at even lower but still sufficiently large flow rates and Reynolds numbers as Kelvin-Helmholtz instabilities in the shear layer of the jet emerging from the pipe. If the flow is buoyancy controlled, instabilities are caused by relatively large toroidal vortices generated on the oxidizer side that periodically "squeeze" the tip of the flame causing its characteristic low-frequency flickering, as shown by Park et al. [25]. They are also of the Kelvin-Helmholtz type but tend to originate further out in the oxidizer stream and are distinct from an additional vortex trail that appears within the luminous flame, when the inner jet flow is transitional [26]. In experiments in jet flames, Davies et al. [8] first found that, as the pressure is raised, evidence of these buoyancy instabilities appear further upstream. This finding was also confirmed in laminar gaseous [9] and spray [10] diffusion flames. An asymptotic analysis of the infinite candle flame [27] also points to a pressure-dependent "flickering" and to a growth rate of the buoyant disturbance with a characteristic length scale that is also pressure-dependent, consistently with these findings.

As mentioned earlier, laminar jet flames are invariably buoyancy-controlled. As a result, the primary concern when operating at high pressures is to avoid buoyancy-induced instabilities. Davies et al. [8] suggested an interesting approach to increase systematically the Richardson number and maintain both Reynolds and Peclet constant by operating at constant mass flow rate as the pressure is raised. In fact, in such a case *Ri* scales with the square of the pressure, since the fuel jet velocity varies inversely with pressure, if the mass flow rate is kept constant. Numerous studies on soot formation at high pressures have been performed at constant fuel mass flow rate (e.g. [7,14]), similarly to [8], which would suggest a progressive increase of the relative importance of buoyancy over inertia. Yet, buoyancy instabilities do not seem to be an issue. The emission of a soot streak is also reported to have a stabilizing effect on the flickering [28]. Stable sooty flames are stabilized because their heights tend to be very modest, on the order of one centimeter, and conditions can be chosen such that buoyant instabilities do not affect the luminous region. As a result, the flames appear to be steady. This is tantamount to lowering the Richardson number in Eq. (1) by reducing the length scale, L. The fact that the flames are no longer as elongated as in the classic Burke-Schuman laminar diffusion flame problem, poses a problem, since the interaction of the flame with the burner mouth becomes important and the modeling of these flames is much more complex in view of the potential for heat/mass losses to the burner rim that are difficult to quantify. There have been even reports of pyrolytic chemistry occurring within the fuel burner [11].

2.2. Counterflow diffusion flames

In contrast with the coflow case, counterflow flames are relatively immune from buoyancy instabilities even if buoyancy plays a role in the positioning of the flame. Typically, opposed-jet burners are designed either with flanges surrounding each jet or with coflows of inert gases that are used to quench the outer periphery of the flame. In the first case, measurements and two-dimensional computational modeling of the flames showed that the flames can be roughly partitioned into two regions: the counterflow region

between the two reactant nozzles, and a radial development region which is initially confined by two recirculation zones that are anchored on the flanges [29]. A systematic investigation revealed that the flame in the first region, that is in the vicinity of the centerline, is immune of buoyancy effects at all but the smallest bulk strain rates, that is for $a < 3.2\ s^{-1}$, where $a = (u_F + u_O)/L$. This value corresponds to $Ri > 15.6$, where Ri is here defined as

$$Ri = \frac{gL^3\Delta T}{v^2\bar{T}} \cdot \frac{v^2}{u^2 d^2} \approx \frac{4g\Delta T}{a^2 d\bar{T}} \tag{2}$$

The second equality stems from the fact that in counterflow $L/d = O(1)$. At these values of a and Ri, the flame is still stable but a small upward shift is observed in the flame position that is caused by buoyancy. In the second region, that is, for radial positions greater than the reactant jet radii, buoyancy does play a role by tilting upward the mixing layer and by affecting the growth of the recirculation zones [29].

In the second counterflow configuration, if the opposed jets are surrounded by inert coflows as opposed to flanges, one would expect that the role played by recirculating bubbles may diminish, as a result of the reduced velocity difference in the shear layer, and they may altogether disappear if the velocity between inner jets and coflow are matched. Still, the otherwise horizontal mixing layer would be tilted upward at a location where the radial velocity component is on the order of a free convective velocity. Buoyancy instabilities would not be expected even in this case, since, if vortical structures were to be generated in the shear layer, they would be convected outwardly, away from the burner centerline, that is the region of interest where most of the measurements/analyses are performed.

The opposed-jet configuration has been reported to be potentially *unstable* with a pitchfork bifurcation with two stable solutions, with the stagnation plane positioned close to either nozzles, and one unstable solution, with the stagnation line halfway between the nozzles, if the momenta of the two jest are matched [30,31]. A probable cause of the instability, as in sudden-expansion flows, is the presence of recirculation bubbles at the exit of the jets when flanges are present. It is likely that the presence of a coflow may have a beneficial influence also in this case. At any rate, except for occasional transients in which the flame may be dramatically displaced from its midpoint position, if the momenta are matched, this hydrodynamic instability has not been found to be an issue from an experimental standpoint.

As a result, the only remaining concern from a stability viewpoint pertains the case in which inertia is controlling and relates to the Re-controlled transition to turbulent flows. Transition is likely to occur within the burner pipe, as a pipe flow, at $Re < 2300$, similarly to what would be experienced in jet flames. We will revisit this point in Section 5.

In conclusion, the counterflow configuration appears to be better suited to reach high pressures, being subject only to the same Re-based restrictions on the laminarity of the flow emerging from the burner nozzle as those of coflow jet flames. Buoyancy-induced instabilities in the latter, on the other hand, constitute a serious obstacle to the establishment of steady flames that cannot be circumvented without introducing additional complications such as heat/mass losses to the burner.

2.3. Steady laminar flames at high pressures

In the context of high-pressure counterflow applications, the highest reported pressure values were in [16], with operation at a fixed strain rate of $30\ s^{-1}$ using 1 cm burner tube up to a pressure of 1.5 MPa, corresponding to an estimated $Re \approx 1500$, well below the transitional value for pipe flow. Not surprisingly, no problems of stability were reported. For the same composition and strain rate under the best of circumstances the flame could be stabilized up to 2.0–2.3 MPa. Still conditions would not be suitable to span the entire pressure range of modern aeroderivative gas turbines that may operate up to 4 MPa. In such a case, the pipe $Re \approx 4000$ and instabilities are likely to set in. One could address this difficulty by carefully contouring the burner nozzles to delay the transition [32], but there are other considerations that may limit the flow rate before the onset of transition, as discussed below.

3. Design criteria and scaling considerations

Listed below are criteria for the stabilization of laminar steady counterflow diffusion flames. They affect the geometry of the burner, the acceptable flow rate range, and, in turn, the strain rate, as well as the transport properties of the streams. Importantly, the pressure at which the flame is established affects the boundaries of the domain in the parameter space within which such flames can be stabilized.The burner diameters, d, of the fuel and oxidizer tubes must measure at least several millimeters to ensure that conditions of self-similarity and, consequently, one-dimensionality are preserved in the neighborhood of the burner centerline. Stability consideration require typically that the burner separation, L be chosen so that $0.5 < L/d < 2$. Larger separations yield flame instabilities, smaller ones are incompatible with adiabatic conditions at the boundary, which is a prerequisite to rely on computational models of these flames that are now routinely available commercially. Although pressure does not affect these geometric parameters, maintaining d small ensures that flow rates and burning rates remain modest, as the pressure is raised. As a result, the management of the experimental system is facilitated with respect to cooling requirements, gaseous consumption, and the extinction of the annular component of the flame surrounding the one-dimensional core by the shroud flow (see below).The Reynolds number must be confined to values well below the transition to turbulence, that is $Re \leqslant Re^c$. Hence,

$$\mathrm{Re} = \frac{ud}{v} = \frac{aLd}{2 \cdot v} \cong \frac{aL^2}{2 \cdot v} < \mathrm{Re}^c \tag{3}$$

where for convenience the mass averaged velocity is expressed in terms of the nominal strain rate a, and the burner separation L as $u = aL/2$. In our experiment $L \cong d$. A $30\times$ or $40\times$ increase in pressure to reach conditions typical of modern gas turbines, increases Re proportionally and may promote instabilities. To maintain Re below its transitional value, one can increase the kinematic viscosity either by preheating the opposed jets or by replacing nitrogen with helium as inert. The first approach is more complex in high-pressure environments and in the case of small burners with inert coflow, but retains the advantage of allowing for operation with mixtures close to those of fuel/air burning. The second is easier to implement, as we did in the present study, at the cost of dealing with more "exotic" mixtures. The use of helium may offer additional advantages from the standpoint of increasing the flame thickness and retaining the flame one-dimensionality.

A pressure increase reduces the flame thickness. The thickness of the thermal mixing layer of a strained diffusion flame δ_T scales as

$$\frac{\delta_T}{\delta_T^0} \approx \sqrt{\frac{\alpha}{a}\frac{a_0}{\alpha_0}} \propto \sqrt{\frac{p_0 \cdot a_0}{p \cdot a}} \tag{4}$$

where α is the mixture thermal diffusivity, p is the pressure, a the strain rate and δ_T^0 a reference thickness. The Full Width Half Maximum (FWHM), the thickness of the temperature profile defined as the shortest distance between two points across the flame where the local temperature gradient is zero, or any other definition can be used in Eq. (4) for δ_T·δ_m can be defined similarly, once the profile

of a given species is considered in place of temperature. The pressure dependence of the flame thickness may preclude detailed probing of the flame structure because the finiteness of the probe volume dimension may reduce the number of measurable data points in the chemically active region of the flame. We can in part compensate for this effect by using helium as inert, as opposed to N_2, and by exploiting the much larger diffusivity of the former. In support of this strategy, we note that in experiments on diffusion flames we reported that helium-diluted flames were much thicker than N_2-diluted ones even when they were operated at much larger strain rates, which should have resulted in thinner structures [33]. This behavior is fully consistent with the scaling in Eq. (4). The replacement of inert should have also beneficial effects with respect to the *species* profile. However, the effect should be less pronounced than that for the thermal layer, because of the relatively large Lewis number of helium mixtures, which will result in smaller gains in effective *mass* diffusivity as compared to the thermal one in Eq. (4).

In conclusion, to ensure a sufficiently broad range of flow rates and compositions for flame stabilization, the preliminary "recipe" emerging from these considerations is that it is advantageous to: (a) use small burners and (b) helium as inert.

4. Experimental setup and procedure

The pressure chamber is designed to operate up to 4 MPa and was hydrostatically tested up to 8 MPa. A threedimensional view of the chamber is shown in Fig. 1, and a schematic of the pressure chamber subsystem is in Fig. 2. The critical component is a $20 \times 20 \times 20\ cm^3$ stainless steel cube, bored with 15.3-cm-diameter perpendicular holes. This configuration offers easy access, relatively large internal volume, and large flanges with the necessary sealing arrangement to host a variety of ports for diagnostics/control (e.g., thermocouples, probes, glass windows, burst disks, etc.). The burner is shown in the inset in figure. It is supported by a translational stage (Velmex X-slide) powered by a (Vexta PK-246) stepper motor, enabling a burner vertical displacement over a 20 mm range with a resolution of 0.01 mm. The lower nozzle is mounted on a *X–Y* translational-rotational stage to allow fine adjustment of the alignment with respect to the fixed upper nozzle. The distance between the nozzles can be varied to ensure adiabatic boundaries for the flame at all experimental conditions. Two chamber extensions house additional components of the system. The lower extension hosts the vertical stage with its electrical connections, the oxidizer, fuel, inert and coflow inlets, and the inlet port of eight thermocouples to monitor the chamber wall temperature. The top extension chamber houses the exhaust outlet, the

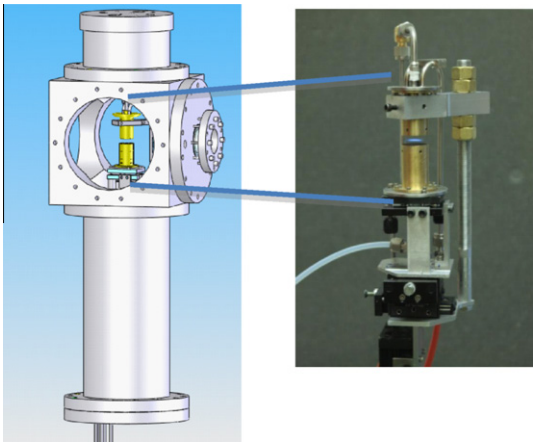

Fig. 1. Schematic of the high-pressure chamber with photograph of the counterflow combustor in the inset. The edge of the stainless steel cube measures 20 cm.

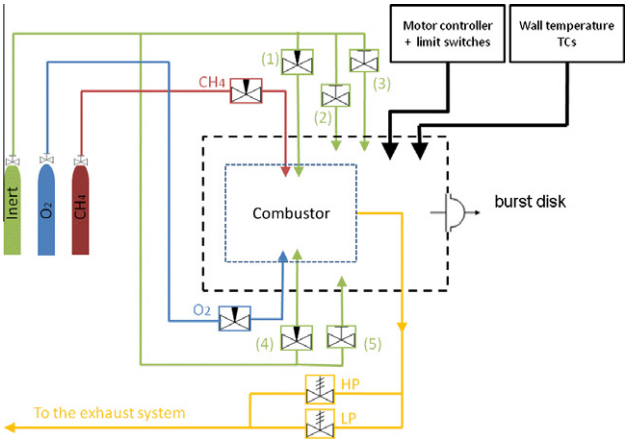

Fig. 2. Schematics of the pressure chamber subsystems: CH_4: methane flow controller; O_2: oxygen flow controller; (1): inert flow controller for fuel dilution; (2): auxiliary inert flow controller; (3): inert flow controller for fuel shroud; (4): inert flow controller for oxygen dilution; (5): inert flow controller for oxygen side shroud; LP: low pressure back-pressure regulator; HP: high pressure back-pressure regulator.

static pressure transducer, the igniter ports and a K-type thermocouple to monitor the exhaust gas temperature. As mentioned earlier, in view of the need to operate the burner at high-pressures and strain rates comparable to those that are used under atmospheric conditions, the burner characteristic dimensions were reduced to limit the total flow rates through the system and the thermal load on the chamber at high pressures. The inlet diameter, d, of the fuel and oxidizer tubes was set at 7.1 mm. Preliminary thermocouple temperature scans showed that the flame is both adiabatic and stable for a burner separation ranging between 6 and 15 mm, corresponding $\sim 1 < L/d < \sim 2$, as typical of this type of burners. Because of buoyancy, hot gases travel quickly to the exhaust and heating of the chamber is minimal, rendering water cooling unnecessary. Since the combustor is not electrically isolated from the experimental bench and the electronics, a glow coil ignition system requiring only 12 V max was preferred to a high voltage spark plug. The igniter port is located in the top extension, and interfaced through a Conax connector, which allows positioning and subsequent extraction from the inlet zone. A sufficiently large shroud flow with a velocity at about 70% of the core jet velocities, is imposed through a diameter of 21.6 mm, requiring a maximum flow rate of 75 slmp per side at 3 MPa. The shroud provision was introduced for the following reasons: first, buoyancy effects in the low strain periphery of the flame tend to cup the flame creating a number of diagnostic difficulties; second, substantial soot production occurs in the low-strain rate region at the flame periphery for some composition of the feed streams, with ensuing experimental complications. With the addition of a robust shroud, the momentum balance between top and bottom shroud flattens the flame and quenches it locally, thereby inhibiting soot formation at the flame periphery (see Fig. 3 below).

Safety is of primary importance in operating a high-pressure device and a number of redundant precautions must be taken to minimize the risk of accidents. The chamber pressure is regulated by a back-pressure regulator but, should the pressure surge be particularly severe, a burst disk is located on the top extension allowing for prompt evacuation of the gas. Window failures are all too common in high-pressure experiments and can be catastrophic if they occur without any early warnings in the way of identifiable cracks. As an additional precautionary measure against glass window failure, the operator is protected by a transparent, bullet-proof (UL 752 Level 1) polycarbonate shield, whereas 8 mm-thick aluminum plates are placed as shields in all other directions. All materials

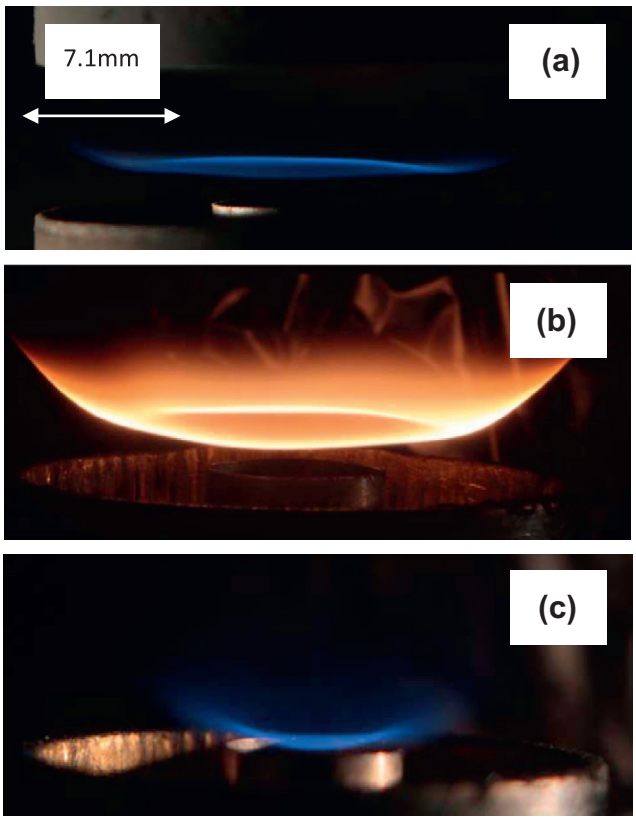

Fig. 3. (a–c) Helium-diluted flames with helium also as a shroud gas: (a) high shroud flow – $Y_{FF} = 0.335$, $Z_{st} = 0.4$, $a = 40/s$, $P = 3$ MPa; (b) low shroud flow – $Y_{FF} = 0.33$, $Z_{st} = 0.41$, $a = 30/s$, $P = 1.8$ MPa; (c) wrinkled flame with similar conditions to those in Fig. 4b ($Y_{FF} = 0.33$, $Z_{st} = 0.41$, $a = 33/s$, $P = 1.8$ MPa) but with the heavier oxidizer stream being fed from the top.

inside the chamber are chosen to be either nonflammable or flame retardant at the maximum operating pressure of 4 MPa and a gas temperature of 373 K. Although the adiabatic flame temperature is much higher than 373 K, inert shrouds ensure enough dilution for all materials to be kept well below their softening temperature. Optical access in the visible is achieved through two 12.7 mm thick BK7 glass windows. The pressurized side of the windows are flushed by warm (373 K) inert to prevent water condensation and soot deposition. A complete schematic of the experimental system is shown in Fig. 2.

Preliminary experiments showed that thermocouples are much too bulky for the small burner dimensions in the high gradient region of the flame and that less intrusive techniques were necessary. By a process of elimination, we excluded Rayleigh thermometry because of its inapplicability in the presence of soot particles, the inevitable stray light complications when dealing with windows, and beam steering that is exacerbated at elevated pressure. As a result, gaseous temperatures between 1200 K and 2300 K were measured via Silicon-Carbide (COI Ceramics, Inc.) thin filament pyrometry [20] using a digital camera (Canon EOS 40D) with a 70 mm f/5.6 lens in the visible range. Because the signal to noise ratio decreases quickly with temperature in the visible range, flames in the low pressure range (0.1–0.8 MPa) were measured also with an infrared camera (Electrophysics PV-320L), equipped with a 50 mm F1.0 Germanium lens, through a 5 mm thick ZnSe window. The infrared camera could not be used above 0.8 MPa because the flame background, whose intensity is proportional to pressure, saturated the sensor and decreased the signal to noise ratio. The technique was calibrated by immersing a Si–C wire in the post flame region of a flat premixed flame whose gas temperature was independently measured with a Pt-Pt10%Rh thermocouple. The thermocouple measurements were corrected for radiative losses and a few data points were successfully validated against computational results for a freely propagating premixed flame using PREMIX. In the temperature range from 1200 to 2300 K, the intensity of the signal increased by a factor $\approx 10^4$, and it was necessary to change the exposure time of the camera depending on the temperature range, between 0.8 s and 1/4000 s. In a temperature interval where calibrations superimpose, some differences in measured temperatures for a given flame were observed. Combining the various errors, the estimated uncertainty in the measured temperatures is at ±40°K. Because calibrations were done in different days, this uncertainty estimate accounts for the repeatability of the calibration setup and any systematic error associated with the measurements. We underline that, despite very low visible signal at low temperature, images of the wire with long exposure time yielded detectable incandescence and limited noise. The blue luminosity from the flame pertains to temperature regions where a short exposure time was used (1/125 s) and was invisible in the wire images, as long as the peripheral part of the flame was kept flat with appropriate shroud flow. At longer exposure times (0.8 and 0.3 s), the importance of the environmental luminosity as source of noise was assessed by measuring the intensity of the wire image outside the flame, which resulted in a negligible signal. Even longer exposure times (2 s) required for lower temperatures resulted in too weak a signal-to-noise ratio.

During temperature measurements no perturbation of the wire to the flame was detected either by naked eye or using a cathetometer. This is not surprising since the wire diameter measures only 13 μm, that is one order of magnitude smaller than the typical size of thermocouples widely used for flame measurements. As mass flow rates scale with pressure, one flow controller per channel cannot cover the entire range of experimental conditions. Each core jet gas flow is controlled by 4 Mass Flow Controllers (MFC), with two additional mass flow controllers for the shroud on each side, for a total of 20 controllers. A set of valves allows for quick switching of the MFCs, depending on the pressure range. The MFC are controlled by two NI boards (PCI-6230) through a Labview visual interface. All flames were stabilized using methane as fuel, and changing the degree of dilution of both fuel and oxidizer streams. Additional experiments (not reported here) were conducted using ethylene.

5. Results and discussion

5.1. Flame quality assessment by visual inspection

We begin with a qualitative discussion of factors that affect flame appearance and position that are typically neglected, even though they can be consequential. To ensure that stability and one-dimensionality were preserved, the relatively small combustor was tested by visual inspection and by thermocouple temperature scans for a variety of experimental conditions. We found that the temperature is uniform in a few mm diameter circle around the centerline, consistently with the anticipated behavior. For all flames, momentum fluxes of oxidizer and fuel streams were approximately balanced to yield a strain rate $a \geqslant 40/s$. Using nitrogen as inert, good quality flames were stabilized up to a pressure of 0.8–1.0 MPa.

Higher pressures should be in principle feasible, since the Reynolds number can be kept well below Re^c. Indeed stable flames could be realized at high pressures, but close examination revealed that they were not uniform in the radial direction. Rather, they exhibited "streaks" originating from the centerline, yielding a petal-like appearance of the flame. This is undesirable, since it violates the condition of one-dimensionality, and therefore of

uniformity in the radial and azymuthal directions, that are critical to use routine computational modeling to complement the experiments. Atmospheric pressure tests on a larger burner that had been realized with a carefully contoured converging section and without using screens or honeycombs showed that similar streaks did not appear up to Re = 1500. Higher flow rates could not be tested for limits in mass flow controller. Therefore, the occurrence of these irregularities is apparatus-specific since it is affected by details of the burner construction, such as the use of screens, honeycombs and other flow conditioning devices. It would appear that $Re \leqslant Re^c$ is not a sufficiently conservative constraint for a counterflow flame of good quality.

Increasing pressure while preserving adiabaticity and therefore a strain rate on the order of at least 10 s^{-1}, increases Re. To avoid the above mentioned radial nonuniformities, it is advantageous to switch to helium as inert, thereby lowering Re. The change of inert leads up to a threefold increase (decrease) in operating pressure (Reynolds number), depending on the composition of the flame, and thus becomes critical to reach the highest pressure (3 MPa) and establish high quality flames. Probably because of its high diffusivity, helium smoothes nonuniformities in the radial direction even when the flame is operated at the same Re as in the petal-like N_2-diluted flame.

Helium had an additional benefit when used also in the shroud flow: it suppresses soot in the peripheral part of the flame more effectively than nitrogen, and decreases the Reynolds number of the shroud flow, both very important effects to obtain a stable and measurable high-pressure flames. A blue 3 MPa flame is shown in Fig. 3a, while the importance of a robust shroud is shown by contrast with Fig. 3b, in which the soot-free flame core is invisible because of soot production in the low strain-rate peripheral region of the flame.

Although the flame was steady and no evidence of buoyancy instability was observed, we found that the some stationary buoyancy effects still persist. In fact, when the denser stream is injected from below, as in (Fig. 3a), the flame is steady, adiabatic and stabilized in a region that is accessible to diagnostic probing. When the configuration is inverted, that is with the denser stream injected from above, the flame is cupped and irregular, and stabilizes almost inside the lower inlet, so that adiabaticity is compromised (Fig. 3c). Because this effect was caused only by switching inlet streams, we attribute it to the relative direction between gravity and the density gradient between the core jets. The equilibrium position of the gas stagnation plane results from the balance of the force between top and bottom jets. Since the jet momenta are approximately balanced and the flame is approximately isobaric, switching feed streams can result in buoyancy-induced shifts in flame position just because of density differences.

We also observed that the flame "floats" with respect to the shroud flow. If a heavy shroud is used, i.e. nitrogen or argon, the flame, although steady, stabilizes very close to the upper inlet and its periphery is quenched very irregularly. A light shroud (helium) stabilizes the same flame closer to the bottom inlet, quenching it evenly. While the flame position appears to be affected by buoyancy, the more uniform quenching may be due to the larger diffusivity of helium. Unfortunately the two effects cannot be decoupled without further testing. Both flame cupping and influence of shroud density appear above ~1 MPa.

We underline that the system could stabilize a blue flame up to 3 MPa, as shown in Fig. 3a. By the same token, incipiently sooting flames can also be studied. Therefore the flame can be employed systematically for a variety of research purposes.

5.2. Thermal layer: measurements and scaling

In Fig. 4 we present temperature measurements for nitrogen-diluted flames at one, two, four and eight atmospheres, respectively (Fig. 4a) and for helium-diluted flames at the same pressure conditions (Fig. 4b) with the same inert used in the shroud flow as in the inner jets. Experimental measurements (symbols) are reported only in the high-temperature region of the flames in which the applied diagnostic technique has sufficient sensitivity, whereas the computational profiles are shown for the entire domain. For all the computations, plug flow conditions were imposed at the boundaries and the profiles where translated along the abscissa to match the peak temperature location, since the model does not take in to account buoyancy-induced shifts. For both sets of flames the burner separation, L, is set to 8 mm. The nitrogen-diluted flames had mass fraction of fuel and oxygen in the respective streams at $Y_{FF} = 0.11$ and $Y_{OO} = 0.49$, respectively. If we define the mixture fraction as $Z = \frac{sY_F - (Y_O - Y_{OO})}{sY_{FF} + Y_{OO}}$, where s is the mass-based oxygen/fuel ratio, this choice corresponds to a stoichiometric mixture fraction $Z_{st} = (1 + sY_{FF}/Y_{OO})^{-1} = 0.53$. The global strain rate, defined as $a = (u_F + u_O)/L$ was kept constant at 60/s. The helium-diluted flames had mass fraction of fuel and oxygen in the respective streams at $Y_{FF} = 0.37$ and $Y_{OO} = 0.98$, respectively, corresponding to a stoichiometric mixture fraction $Z_{st} = 0.40$. Their global strain rate was kept constant at $a = 150$/s. For all flames, momentum fluxes of fuel and oxidizer jets were the same, implying that, for helium-diluted flames since the oxidizer stream is denser, the oxidizer velocity was typically one half that of the fuel stream. For nitrogen-diluted flames, the velocity of the two opposed jets is almost equal. The strain rate of the helium-diluted flame was kept high to limit the flame thickness and preserve adiabatic boundary conditions.

As anticipated, on the basis of the scaling consideration discussed above (see Eq. (4)), as the pressure is raised at constant strain rate, the profiles become narrower and the peak temperature increases in either set of flames, as a result of radical recombination and adiabatic flame temperature considerations. The computed profiles are invariably narrower as compared to the experimental ones by roughly 20% but in good agreement with respect to the peak temperature that differs at most by 70 K with respect to the measured values. Despite this discrepancy, infrared measurements up to 0.8 MPa were in very good agreement with visible measurements. Although the pressure was varied by nearly one order of magnitude, it was not possible to increase it further

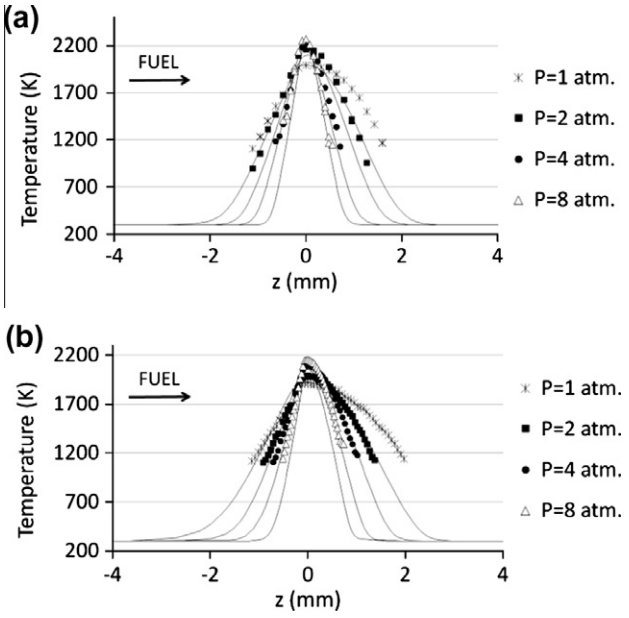

Fig. 4. Experimental and computational temperature profiles in a) nitrogen-diluted flames ($Y_{FF} = 0.11$, $Z_{st} = 0.53$, $a = 60$/s) and helium-diluted flames ($Y_{FF} = 0.37$, $Z_{st} = 0.40$, $a = 150$/s) at 0.1, 0.2, 0.4 and 0.8 MPa, respectively.

because of high soot loading in the low strain rate, peripheral part of the flame. The high shroud velocity required to preserve high strain, dilute the composition locally and eliminate soot, destabilized the flame. To expand the pressure range further, we chose a more diluted flame with $Y_{FF} = 0.355$, $Y_{OO} = 0.944$, and $Z_{st} = 0.40$, whereas the burner spacing was reduced to 6 mm, resulting in lower mass flow rate and a reduction in the extent of the peripheral flame for a given strain rate. To preserve adiabaticity, the pressure-weighted strain rate was kept constant, that is $p \cdot a = 32.0$ MPa/s while the pressure was varied between 0.2 and 0.8 MPa. As the pressure is raised, the flame becomes thinner, which can be compensated by a corresponding decrease in strain rate. As a result, we anticipate that these flames should have comparable thickness based on the scaling of Eq. (3). Indeed that is the case, as shown in Fig. 5. The two-atmosphere flame has the highest strain rate at 160/s and is approaching extinction, as shown by the relatively low peak temperature.

Extending the pressure range at much higher pressures and maintaining constant $p \cdot a = 32.0$ MPa/s is not possible since the strain rate would have been too low and the flame would be relatively unstable. Therefore, for a second set of flames we kept the strain rate constant at $a = 40$/s and varied the pressure from 0.8 to 3.0 MPa. Data in Fig. 6 show the same general trends as discussed for Fig. 4, although the variation in peak temperature is more modest than in the lower temperature range.

To check the applicability of the scaling considerations in Section 3, we rescaled the temperature profiles as follows. In the ordinate we plotted the reduced temperature $\frac{T-T_0}{T_{MAX}-T_0}$ [34], where T_0 is the temperature at the (cold) boundary and T_{MAX} the peak temperature. The abscissa, on the other hand, is non-dimensionalized as z/δ_{diff} with the denominator chosen as the thermal mixing layer characteristic thickness defined as $\delta_{diff} = \sqrt{\frac{\alpha_0}{a_{ox}}\frac{p_0}{p}}$. α_0 is an effective thermal diffusion coefficient at atmospheric pressure and the global strain rate previously defined is computed with the average velocity of the oxidizer stream as $a_{ox} = 2u_{ox}/L$, since the helium-diluted flames lie on the oxidizer side of the stagnation plane. This choice has no influence on the rescaling of nitrogen-diluted flames, since they have almost equal jet velocity. The thermal diffusivity of the oxidizer stream mixture is computed at a mean temperature of 1000 K [35]. Because both helium-diluted flames contain a high mole fraction of oxygen in the oxidizer stream, the transport properties are very different from those of pure helium. In the nitrogen-diluted flames, on the other hand, transport properties are barely affected by the presence of either oxygen or methane. Rescaled profiles are shown in Fig. 7 exhibiting good collapse among all flames despite the fact that the original profiles in Figs. 4–6 showed width variations by a factor of 3. As for the thermal layer, we expect some gain in the chemical layer thickness as well. In fact,

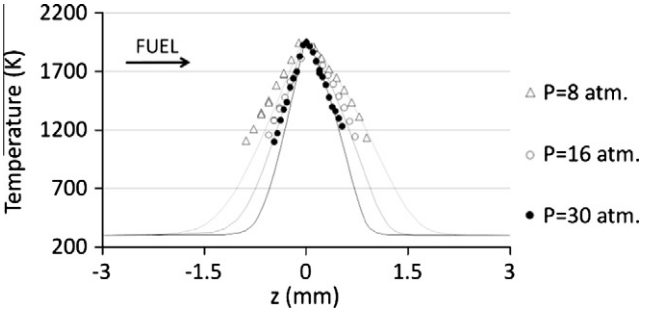

Fig. 6. Experimental and computational temperature profiles in helium-diluted flames ($Y_{FF} = 0.355$, $Z_{st} = 0.4$, $a = 40$/s, at $P = 0.8$, 1.6 and 3.0 MPa, respectively.

$$\frac{\delta_m|_{He}}{\delta_m|_{N_2}} = \sqrt{\frac{D^0_{He}}{a_{He}}\frac{p_0}{p_{He}}} \Big/ \sqrt{\frac{D^0_{N_2}}{a_{N_2}}\frac{p_0}{p_{N_2}}} \tag{5}$$

To eliminate arbitrariness in the selection of diffusivities, we can compute the l.h.s. of Eq. (5) numerically, use the bulk strain rate on the oxidizer side for consistency with the temperature profiles rescaling, and infer $D^0_{He}/D^0_{N_2}$ where the zero superscript refers to atmospheric pressure conditions. For the helium-diluted case with $Y_{FF} = 0.355$, the ratio is 1.5, while for the $Y_{FF} = 0.37$ case the ratio is 1.2. These values lead to an increment of the chemical layer thickness δ_m by a factor 1.22 and 1.1, respectively.

5.3. Domain of well behaved flames

Fig. 8 shows a graphical representation of the operational domain of the burner with the diffusion layer thickness δ, plotted versus the pressure-weighed strain rate $(a \cdot p)$. These variables were normalized with the corresponding quantities from a computed nitrogen-diluted flame with: $L = 8$ mm, $a_0 = 60/s$, $p_0 = 0.1$ MPa, $Y_{FF} = 0.11$, $Y_{OO} = 0.4$ and $Z_{st} = 0.53$, and $\delta^0_T|_{N_2} = 6$ mm, with the same notation used in Section 5.

The adiabaticity condition is then expressed as

$$\frac{\delta_T}{L} < 0.9 \Rightarrow \frac{\delta_T}{\delta^0_T|_{N_2}} < 1.2 = \left(\frac{\delta}{\delta^0_{N_2}}\right)_{\substack{MAX \\ adia}} \tag{6}$$

As previously explained, Eq. (4) scales profiles well when the bulk strain rate on the oxidizer side is used, and, for the helium case, an appropriate diffusivity is used. The diffusion layer thickness for the nitrogen-diluted case is plotted as a continuous black curve, whereas two curves are needed for the helium-diluted case because of non-unity Lewis number, one for the thermal layer (continuous blue (grey in the printed version) curve), the other for the mass diffusion layer (dotted blue curve). Limit values for the abscissa are

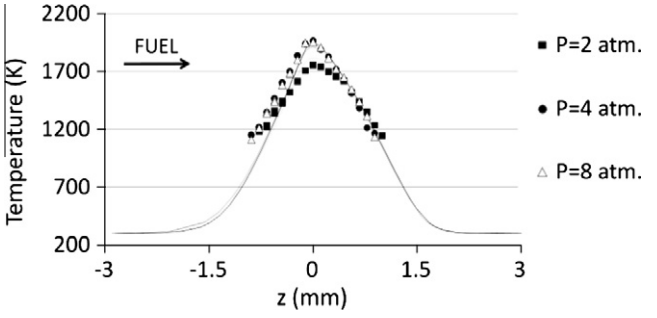

Fig. 5. Experimental and computational temperature profiles in helium-diluted flames ($Y_{FF} = 0.355$, $Z_{st} = 0.4$, $P \cdot a = 32.0$ MPa/s, at $P = 0.2$, 0.4 and 0.8 MPa, respectively.

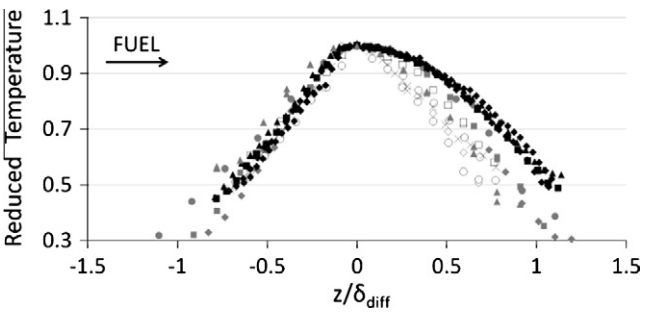

Fig. 7. Rescaled temperature profiles from Figs. 4–6. Gray symbols: nitrogen-diluted flames. Black open symbols: helium-diluted flames, $Y_{FF} = 0.355$. Black full symbols: helium-diluted flames, $Y_{FF} = 0.37$.

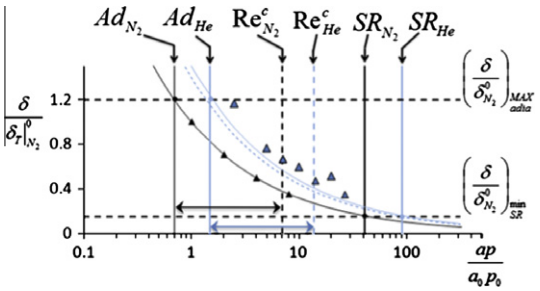

Fig. 8. Mixing layer thickness and pressure weighed strain rate normalized with values from a particular flame. Black and light blue (grey in the printed version) symbols/lines refer to nitrogen-diluted flames and helium-diluted flames, respectively. The double arrowed horizontal line defines the domain of well behaved flames for the two diluents. See text for details.

found at the intersection between the horizontal line $\delta/\delta^0_{N_2} = 1.2$ and curves of the flame thermal thickness, setting the lowest allowed value for $(p \cdot a)/(p_0 \cdot a_0)$ at 0.7 for nitrogen and 1.3 for helium. These locations set by adiabaticity constraints are marked with vertical continuous lines labeled Ad_{N_2} and Ad_{He}, respectively.

The spatial resolution limit is expressed as:

$$\frac{\delta_m}{\delta^0_T|_{N_2}} > \frac{N\sigma}{\delta^0_T|_{N_2}} = \left(\frac{\delta}{\delta^0_{N_2}}\right)_{\substack{\min \\ SR}} = 0.16 \tag{7}$$

where $N = 10$ is the selected number of minimum sampling locations and $\sigma = 0.1$ mm is the assumed best spatial resolution for some of the diagnostics to be used (e.g., gas sampling for chemical analytical instrumentation). This constraint is represented by an horizontal dotted line in Fig. 8. Intersections of this horizontal line with the mass diffusion layer thickness curves yield the upper limits for $(p \cdot a)/(p_0 \cdot a_0)$ at 36 for nitrogen and 91 for helium , respectively, and are marked as vertical continuous lines labeled SR_{N_2} and SR_{He} , respectively.

The critical Reynolds Re^c for streaks appearance was conservatively set at 750, even though loss of flame quality is progressive, and the value is apparatus-specific. It is likely that with contoured burned design this limit may be increased by a factor of two. This limit implies that $(p \cdot a)/(p_0 \cdot a_0) < 7$ for the nitrogen case and is denoted with a vertical dotted line labeled $Re^c_{N_2}$. In the case of helium-diluted flames, the balanced momenta condition implies that the oxidizer inlet velocity is lower than the fuel one. For the $Y_f = 0.355$ case, $a_{ox} = 0.67a$ and for $Y_f = 0.37$, $a_{ox} = 0.6a$ where $a = \frac{(u_f + u_{ox})}{L}$ and $a_{ox} = \frac{2u_{ox}}{L}$. Since in our flames the higher Reynolds number is found on the oxidizer side, the critical Reynolds limit is expressed as: $Re^c = u_{ox} L \rho_{ox}/\mu_{ox} = 0.6 * aL^2 \rho_{ox}/(2\mu_{ox})$ which, in terms of the abscissa becomes:

$$\frac{ap}{a_0 p_0} = \frac{2Re_{cr} R_0 T \mu^{300^\circ K}_{ox}}{0.6 Mw_{ox} L^2 a_0 p_0} \approx 13 \tag{8}$$

and is marked by the vertical dotted line labeled Re^c_{He}. It is important to consider the difference in velocity between the two streams, or the benefits of helium would not be evident.

Finally, we plotted the numerical thickness for the nitrogen-diluted flames (black triangles) and for the helium-diluted ones (blue triangles), and obtained good agreement with the thickness curves, consistently with the good rescaling results in Fig. 7. The numerical thermal thickness was computed using Oppdif as the shortest distance between two points across the flame where the local temperature gradient is zero. We notice that in all cases adiabaticity was preserved and the limiting upper value in pressure-weighted strain rate is set by Re^c rather than by spatial resolution constraints. Although this value was exceeded by two helium-diluted flames, thin filament pyrometry showed that at a given axial location, the temperature was radially uniform across a few millimeters around the centerline, which confirmed that the selected criteria are very conservative. As a summary, the pressure-weighed strain rate ranges that are accessible and result in well behaved flames are marked with two horizontal double-arrow lines, color-coded with respect to the chosen diluent, that are positioned near the abscissa and partially overlap.

6. Conclusions

We presented an experimental system capable of stabilizing counterflow diffusion flames up to at least 3.0 MPa. This configuration produces well-controlled, steady flames, that, depending on the feed stream composition, can be soot-free or moderately sooting. The substitution of helium as inert in place of nitrogen is essential to stabilize a flat flame above 1 MPa by avoiding non-homogeneities that would otherwise compromise the flame one-dimensionality. Helium in the coflow is also effective at suppressing strong soot formation in the peripheral, low-strain part of the flame at pressures above 1.5 MPa. This annular soot would cloud observation of the flame core. We presented scaling laws to define a regime of diffusion flames of good quality with respect to adiabaticity, laminarity, stability, one-dimensionality and spatial resolution. A limit plot is identified to realize these conditions and synthesize constraints on two operating variable at the experimentalist disposal: pressure and strain rate. The plot can provide guidance for the design of counterflow system with respect to the geometrical parameters of the combustor and the choice of the experimental conditions.

Helium dilution was critical to preserve the flame one-dimensionality, by delaying the appearance of flame irregularities (streaks), allowing the stabilization of flames up to 3.0 MPa and had a limited effect on flame thickness.

Acknowledgments

The authors gratefully acknowledge the financial support of NSF (Grant #CBET-0651906, Dr. Arvind Atreya, Program Director) and of the Air Force Office of Scientific Research (Grant # FA9550-06-1-0018, Dr. Julian Tishkoff, Program Manager) and the help of Mr. Nick Bernardo in the construction of the hardware.

References

[1] W.L. Flower, C.T. Bowman, Proc. Combust. Inst. 27 (1984) 1035–1044.
[2] W.L. Flower, Combust. Sci. Technol. 37 (1986) 31–43.
[3] W.L. Flower, C.T. Bowman, Proc. Combust. Inst. 21 (1986) 1115–1124.
[4] W.L. Flower, C.T. Bowman, Combust. Sci. Technol. 37 (1994) 93–97.
[5] L. McCrain, W.L. Roberts, Combust. Flame 140 (2005) 60–69.
[6] K.A. Thomson et al., Combust. Flame 140 (2005) 222–232.
[7] H.I. Joo, O.L. Gulder, Combust. Flame 157 (2010) 1194–1201.
[8] R.W. Davis et al., Combust. Sci. Technol. 73 (1990) 625–635.
[9] H.G. Darabkhani et al., Fuel 88 (2009) 264–271.
[10] S. Russo, A. Gomez, Combust. Flame 145 (2006) 339–356.
[11] M.R.J. Charest et al., Proc. Combust. Inst. 33 (2011) 549–557.
[12] D.X. Du, H. Wang, C.K. Law, Combust. Flame 113 (1998) 264–270.
[13] C.J. Sun et al., Proc. Combust. Inst. 26 (1996) 1111–1120.
[14] C.J. Sung et al., Proc. Combust. Inst. 27 (1998) 1523–1529.
[15] H. Bohm, F. Lacas, Proc. Combust. Inst. 28 (2000) 2627–2634.
[16] R.V. Ravikrishna et al., Combust. Sci. Technol. 176 (2004) 1–21.
[17] K. Maruta et al., Proc. Combust. Inst. 31 (2007) 1223–1230.
[18] M.D. Smooke et al., Combust. Flame 147 (2005) 613–628.
[19] R.J. Kee et al., CHEMKIN Release 4.1.1, Reaction Design, San Diego, CA, 2007.
[20] V. Vilimpoc, L.P. Goss, Proc. Combust. Inst. 22 (1988) 1907–1914.
[21] G.P. Smith et al., <http://www.me.berkeley.edu/gri_mech/>.
[22] F.G. Roper, Combust. Flame 29 C (1977) 219–226.
[23] F.G. Roper, Combust. Flame 29C (1977) 227–234.
[24] F.A. Williams, Combustion Theory, Westview Press, Boulder, CO, 1985.
[25] Park et al., Combust. Flame 99 (1994) 767–774.
[26] L.D. Chen et al., Proc. Combust. Inst. 22 (1986) 677–684.
[27] J. Buckmaster, N. Peters, Proc. Combust. Inst. 21 (1988) 1829–1836.
[28] V.R. Katta et al., Proc. Comb. Inst. 32 (2009) 1343–1390.

[29] G. Amantini et al., Combust. Flame 147 (2006) 133–149.
[30] R.P. Pawlowski et al., J. Fluid Mech. 551 (2006) 117–139.
[31] J.C. Rolon et al., Exp. Fluids 11 (1991) 313–324.
[32] T. Morel, J. Fluid. Eng. 97 (1975) 225–233.
[33] A. Gomez, D.E. Rosner, Combust. Sci. Technol. 89 (1993) 335–362.
[34] L. Pons, N. Darabiha, S. Candel, Combust. Flame 152 (2008) 218–229.
[35] R.C. Reid, J.M. Prausnitz, B.E. Poling, The Properties of Gases and Liquids, McGraw-Hill, New York, NY, 1987.